Future Technology
Open Access Journal
ISSN 2832-0379

May 2026| Volume 05 | Issue 02 | Pages 159-165
Journal homepage: https://fupubco.com/futech
https://doi.org/10.55670/fpll.futech.5.2.15

Future Publishing LLC

Article

Boosting organic pollutants degradation by surface defects of iron oxide nanofibers

Yingying Ma*

California Institute of Technology, Pasadena, CA 91125, United States

ARTICLE INFO

Article history:
Received 22 October 2025
Received in revised form
24 December 2025
Accepted 29 January 2026

Keywords:
Pollutants degradation, Defects,
Iron oxide nanofiber, Oxygen vacancy

*Corresponding author
Email address:
yymaedu@163.com

DOI: 10.55670/fpll.futech.5.2.15

ABSTRACT

The release of organic dyes is a serious concern to the water resources and the quality of the environment, and there is a strong necessity to create effective catalysts that can degrade organic dyes. Here, the nanofibers of iron (III) oxide were produced using the electrospinning technique and the high-temperature firing technique, and the oxygen vacancy defects on the surfaces of the nanofibers were formed using the reduction technique of NaBH4. The findings show that the surface oxygen vacancies significantly enhance the catalytic activity. Specifically, the Fe2O3−VO nanofibers achieved near-complete degradation of MB within 4 minutes, with a reaction rate constant (k≈0.95 min-1) approximately 68 times higher than that of pristine nanofibers. Such optimized properties not only demonstrate the potential of defect-engineered iron oxide in organic dye treatment but also provide insights into the structural design of highly effective catalysts for sustainable water remediation.

1. Introduction

In industrial production, organic dyes like methylene blue (MB) and rhodamine B (RhB) have found wide applications [1,2]. Nevertheless, the wastewater of these processes still possesses a high concentration of undecomposed dye molecules and other organic pollutants, which are highly chromatic and chemically reactive. During the discharge of industrial dye wastewater, the organic contents of the wastewater can penetrate the soil, which impacts the fertility of the soil as well as biodiversity, and even enter into groundwater systems and trigger groundwater pollution [3]. Treating wastewater from industrial dyes is very important in securing the environment and human health [4,5]. This has resulted in the emergence and use of eco-friendly dyes and effective wastewater treatment technologies becoming more relevant [6]. Such common methods of treatment are biodegradation [7], catalytic oxidation [8], photocatalysis [9], ion exchange [10], and membrane separation [11] technology. Such methods are capable of degrading and eliminating dangerous substances in dye wastewater to minimize the effects of the wastewater on the environment. One of the methods that uses catalysts to enable the oxidation reaction is known as chemical catalytic oxidation, which finds extensive application in chemical synthesis, wastewater remediation, and environmental protection [12,13]. The choice of a catalyst is also a vital part of catalytic oxidation. Examples of common catalysts used in chemical catalysis would be metal catalysts, oxide catalysts, acid-base catalysts, and enzyme catalysts [14,15]. Of these, transition metal oxide catalysts are important especially. These catalysts find frequent application in oxidation reactions, redox reactions, and catalytic cracking processes [16,17]. The catalysts are transition metal oxides, which have high activity and selectivity and so catalyze a wide range of complex reactions, including oxidation, hydrogenation, and reduction of oxygen. The oxidation states of the elements of the transition metals, as well as the exceptional characteristics of their crystal structure. Typical examples of the transition metal oxide catalysts are iron oxides, cobalt oxides, and nickel oxides [18,19]. The catalysts are of great importance in the industrial context, including organic synthesis, environmental protection, and energy conversion [20,21]. There are many benefits of chemical catalytic oxidation. To begin with, catalysts may decrease the activation energy of the reaction, raise the rate of reaction, and in some instances, improve the selectivity of the product, thus minimizing the formation of by-products. Secondly, catalytic oxidation reactions are usually lower in temperature and pressure as opposed to non-catalytic oxidation reactions, conserving energy and minimizing costs of operation. Also, the reusability of catalysts leads to both an increase in the service life of catalysts and a decrease in waste production, which is a part of the environmental sustainability aims. Iron oxide (Fe_2O_3) is a very popular catalyst because it has a lot of benefits. Iron oxide has great catalytic properties, and thus it can drive numerous significant chemical processes, including oxidation, hydrogenation, and catalytic cracking [22,23]. The catalyst is very stable in different circumstances, and it retains its catalytic activity over a long period, lowering the rate of deactivation of the catalyst. Also, iron oxide catalysts are renewable; the catalytic efficiency of these catalysts can be restored by using simple treatment or regeneration processes, thus increasing their lifespan. Iron oxide is more environmentally friendly than other catalysts since the raw materials that are used in its preparation tend to be relatively common and do not pose serious environmental hazards [24,25]. Due to its exceptional qualities, iron oxide catalysts have found extensive application in the field of organic synthesis, environmental protection, and energy conversion, offering efficient catalytic activity on a wide range of significant reactions.

Oxygen vacancy (V_O) defects offer significant advantages in catalysis by enabling the tuning of surface structures and chemical properties [26], providing new strategies for developing efficient and selective catalysts. Firstly, $V_O$sites provide additional active centers that adsorb and activate reactant molecules, increasing the contact area and reaction rate [27]. Secondly, these defects modulate the catalyst's electronic structure, altering reactant interactions and reaction selectivity [28]. For instance, $V_O$can partially modify surface activity to favor specific pathways like reduction. Moreover, $V_O$defects can stabilize reaction intermediates, further promoting the catalytic process. Importantly, $V_O$concentration and distribution are controllable through preparation conditions, allowing for precise activity regulation. However, research on the specific role of surface $V_O$in iron oxide nanofibers for oxidative dye degradation remains limited. Therefore, this study aims to: (1) synthesize 1D Fe_2O_3nanofibers with an engineered surface $V_O$using a $NaBH_4$reduction strategy; (2) systematically characterize these defects; and (3) evaluate their efficiency in activating peroxymonosulfate (PMS) to degrade organic dyes (MB and RhB). By establishing a clear structure-activity relationship, this work provides insights into designing high-performance, defect-rich catalysts for water remediation.

2. Authorship and contribution

2.1 Preparation of iron oxide nanofibers and construction of surface defects

Fe_2O_3 nanofibers were synthesized via electrospinning followed by high-temperature calcination. Initially, 1.5 g of iron (III) acetylacetonate (Fe(acac)$_3$), 1.5 g of polyacrylonitrile (PAN), and 12 g of N, N-dimethylformamide (DMF) were stirred in a conical flask at 60°C for 12 hours to obtain a uniform precursor solution. The solution was then transferred to a 10 mL syringe equipped with a 20G needle. Electrospinning was performed at 16 kV with a 20 cm collection distance, maintained at 25°C ± 2°C and 35% ± 5% humidity. These optimized parameters ensured a stable Taylor cone and bead-free fiber formation. The resulting PAN/Fe(acac)$_3$ fibers were calcined in a muffle furnace at 500°C (5°C·min^{-1} heating rate) in air for 1 h to ensure crystallization, then naturally cooled to room temperature.

To construct oxygen vacancy (V_O) defects, a $NaBH_4$ reduction method was employed. 50 mg of Fe_2O_3 nanofibers were ultrasonically dispersed in 25 mL of deionized water for 5 minutes. Subsequently, 50 mg of $NaBH_4$ was added, and the mixture was stirred at 500 rpm for 1 hour. The product was collected by centrifugation, washed repeatedly with deionized water and ethanol, and vacuum-dried at 60°C for 12 hours to obtain Fe_2O_3-V_O nanofibers.

2.2 Structural characterization and catalytic performance

The microstructure of the catalyst was characterized by scanning electron microscopy (SEM, JEOL JSM-7800F, Japan) at an accelerating voltage of 15 kV, and transmission electron microscopy (TEM, FEI Tecnai G2 F20, USA) at 200 kV. The crystalline structure was ascertained using X-ray diffraction (XRD, Rigaku SmartLab, Japan) with Cu Kα radiation (λ=1.5418 Å). The specific surface area was measured by the Brunauer-Emmett-Teller (BET) method via nitrogen physisorption on a physical adsorption instrument (Micromeritics ASAP 2460, USA). Electron paramagnetic resonance (EPR, Bruker EMXplus, Germany) and X-ray photoelectron spectroscopy (XPS, Thermo Scientific K-Alpha, USA) were employed to study the electronic structure.

2.3. Catalytic Oxidative degradation of Organic Dyes

To prepare stock solutions, 12.5 mg of methylene blue (MB) was dissolved in 30 mL of deionized water using a glass rod and then diluted to 250 mL in a volumetric flask to reach 50 mg L^{-1}. Rhodamine B (RhB) and potassium peroxymonosulfate (PMS, 0.5 mg L^{-1}) solutions were prepared following the same procedure. In a typical oxidation process, 25.0 mL of MB solution was mixed with 5.0 mg of catalyst (Fe_2O_3 or Fe_2O_3-$V_{(O)}$). This dosage (0.2 g/L) was selected based on prior studies and our preliminary screening to balance catalytic efficiency and economic cost; higher dosages may lead to particle aggregation and light scattering interference. The reaction started immediately upon adding 300 μL of PMS. 200 μL samples were collected every 4 minutes and analyzed by a UV-Vis spectrophotometer at 664 nm (MB) and 554 nm (RhB). RhB degradation followed the same protocol. All experiments were performed in triplicate to ensure reproducibility, with a relative standard deviation (RSD) below 5%.

3. Results and discussion

After electrospinning and calcination, a red sample was obtained, as shown in Figure 1, which was consistent with the color of iron oxide. The resulting iron oxide was put into water by ultrasonic stirring, and the solution was red. The solution slowly turned black after adding $NaBH_4$ solution, and the solid product was centrifuged, washed, and dried after sufficient reaction for 1 hour to obtain the black sample shown on the right side of Figure 1. This distinctive color transition from red to black serves as a visual indicator of the surface reduction process. While qualitative, the formation of surface oxygen vacancies (V_O) was further confirmed and quantified by subsequent characterizations; specifically, XPS analysis (Figure 6) revealed a significant increase in the defective oxygen (O_D) percentage from 31.8% to 76.6%, and EPR spectra (Figure 5) showed a substantially enhanced signal at g=2.002. The morphology and structure of Fe_2O_3 were characterized, and the results are shown in Figure 2. From the characterization results, it can be found that the Fe_2O_3 obtained after calcination still has a homogeneous morphology (Figure 2a) with a fibrous structure. The high-magnification cross-sectional SEM image shows that Fe_2O_3 exhibits a thin-walled hollow structure with folds on the surface (Figure 2b), and the TEM characterization results further confirm the existence of the folds and the thin-walled hollow structure (indicated by arrows in Figure 2c). The average diameter of Fe_2O_3 nanofiber obtained from statistical calculation was 608 ± 92 nm (based on the measurement of 100 randomly selected fibers from SEM images) (Figure 2d). The morphology of Fe_2O_3-VO obtained after reduction using $NaBH_4$ still maintains the fibrous structure, which is consistent with the morphology of Fe_2O_3 nanofiber before reduction.

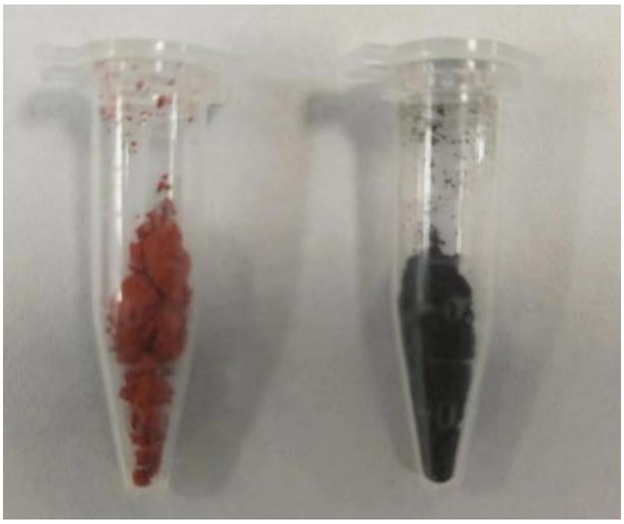

Figure 1. Digital photographs of the resulting Fe_2O_3 nanofibers (left) and oxygen-containing vacancies Fe_2O_3 (right)

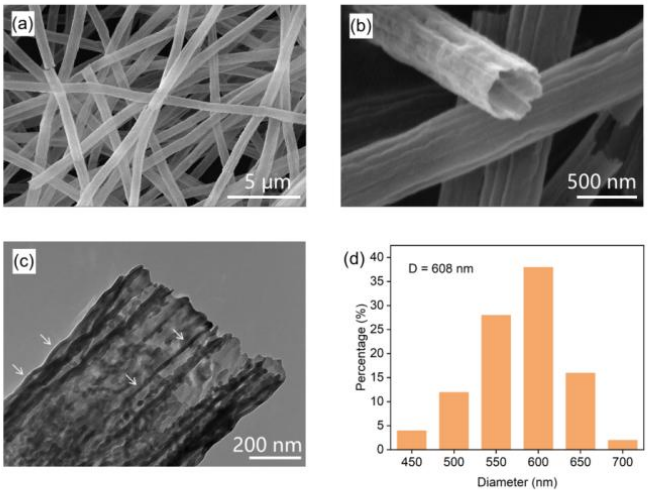

Figure 2. Morphological characterization and diameter of Fe_2O_3nanofibers. (a-b) Cross-section SEM images of Fe_2O_3 nanofibers, (c) TEM images of Fe_2O_3 nanofibers, (d) Statistical calculated diameter of Fe_2O_3 nanofibers (Average diameter = 608 ± 92 nm, measured from n = 100 fibers).

Subsequently, The N2 adsorption and desorption curves, specific surface area and pore size distribution of Fe_2O_3 were characterized using a physical adsorption instrument, and the results are shown in Figure 3. Fe_2O_3 showed a type IV adsorption and desorption isomer, with a specific surface area of about 37.99 $m^2 \cdot g^{-1}$, and the pore size distribution was concentrated near 2-3 nm, i.e., the pore structure in Fe_2O_3 was dominated by mesopores. Similarly, the adsorption characteristics of Fe_2O_3-V_O are consistent with those of Fe_2O_3 nanofibers, and the specific surface area does not change significantly. This indicates that the oxygen vacancies generated by $NaBH_4$ reduction are atomic-scale point defects. These defects modify the surface chemical state but are too small to significantly alter the mesoporous structure or the total specific surface area accessible to N_2 molecules. This stability in surface area further confirms that the enhanced catalytic performance is driven by the increased density of active sites (V_O) rather than physical morphological changes. X-ray diffraction (XRD) was employed to analyze the crystal phases of $Fe_2O_3$and Fe_2O_3-$V_O$nanofibers (Figure 4). Both samples exhibit distinct diffraction peaks at 24.1°(012), 33.2°(104), 35.6°(110), and 40.9°(113), indexing to the hematite α-Fe_2O_3phase (JCPDS No. 33-0664, space group: R-3c) [29]. This confirms that the V_O construction process did not induce a significant phase transition. This stability is attributed to the mild liquid-phase reduction, where BH_4^-anions strip surface lattice oxygen and reduce adjacent $Fe^{3+}$to $Fe^{2+}$to maintain charge neutrality. However, room-temperature kinetics are insufficient to trigger the atomic rearrangement required for a bulk transformation to Fe_3O_4or metallic Fe, restricting defects primarily to the surface. Notably, the peak intensities of Fe_2O_3-$V_O$show a clear decrease compared to Fe_2O_3, reflecting reduced surface crystallinity following $V_O$introduction. Although Raman spectroscopy was not performed, the absence of impurity peaks in the XRD pattern, combined with surface chemical changes observed in XPS and EPR, confirms that $NaBH_4$treatment successfully engineered surface oxygen vacancies without altering the bulk α-Fe_2O_3crystalline phase.

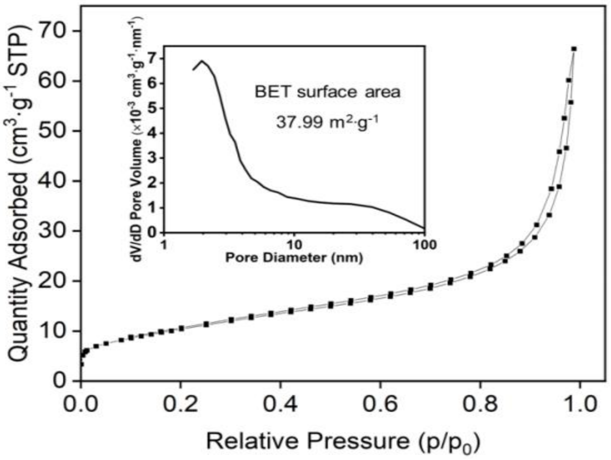

Figure. 3 Specific surface area and pore size distribution of Fe_2O_3 fiber

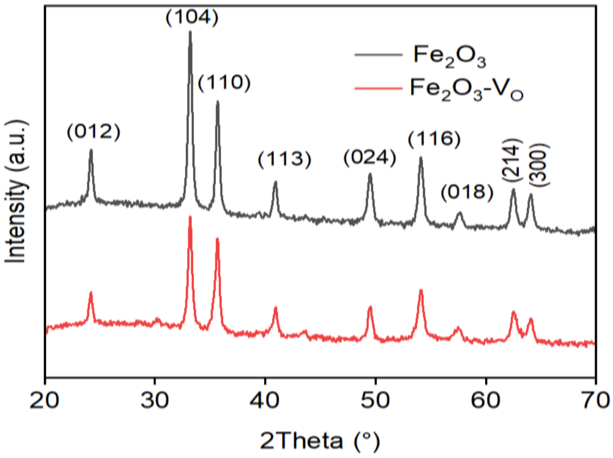

Figure 4. XRD characterization results of the samples

EPR was then used to characterize the oxygen vacancy defect V_O. From the characterization results of EPR, it can be seen that the signal near g = 2.002 is characteristic of electrons trapped in oxygen vacancies (V_O). This sharp resonance is distinct from the broad signals typically associated with bulk ferromagnetic iron species, which appear at different fields. The specific g-value of 2.002 is widely accepted in literature as a fingerprint for surface oxygen vacancies in metal oxides [30, 31]. Due to the reduction of $NaBH_4$, there is a significant increase in the concentration of V_O in the sample from Fe_2O_3 nanofibers to Fe_2O_3-V_O (Figure 5). From Figure 5, it can be seen that a small amount of V_O also exists in the Fe_2O_3 nanofibers, and these oxygen vacancy defects mainly come from the bulk intrinsic defects generated during the calcined PAN/Fe(acac)$_3$ preparation of Fe_2O_3, while the increase in the signal intensity of V_O in Fe_2O_3-V_O is very obvious, indicating that the increase in the concentration of oxygen vacancy defects in Fe_2O_3-V_O is significant, which comes from the $NaBH_4$ reduction process.

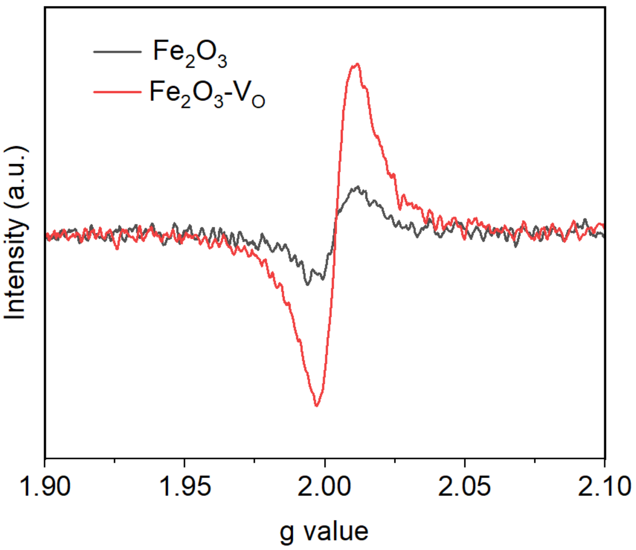

Figure 5. EPR characterization results of the samples

Subsequently, X-ray photoelectron spectroscopy (XPS) was employed to further confirm the oxygen vacancy defects. All XPS spectra were calibrated using the C 1s peak at 284.8 eV. A Shirley-type background was subtracted, and the peaks were fitted using a Gaussian-Lorentzian mixed function (GL (30)). The O 1s spectra were deconvoluted into two components: lattice oxygen (O_L) at ~529.5 eV and defective oxygen (O_D) at ~531.2 eV. As shown in Figure. 6a, the split-peak fitting results from the O 1s XPS fine spectra of Fe_2O_3 nanofibers and Fe_2O_3-V_O revealed the presence of characteristic peaks in the samples corresponding to OL (lattice oxygen) species and OD (defective oxygen) species [32, 33]. In Fe_2O_3 nanofibers, the percentage of OD is 31.8%, while in Fe_2O_3 -V_O the percentage of OD increases from 31.8% to 76.6% and the percentage of OL decreases from 68.2% to 23.4% (Figure 6), indicating a significant increase in the concentration of V_O in Fe_2O_3 -V_O. It is worth noting that XPS is a surface-sensitive technique (probing depth < 10 nm). Therefore, this high percentage (76.6%) reflects the extremely high density of oxygen vacancies specifically in the outermost surface layers induced by the $NaBH_4$ reduction, rather than the bulk stoichiometry. This result is also consistent with the results obtained by EPR.

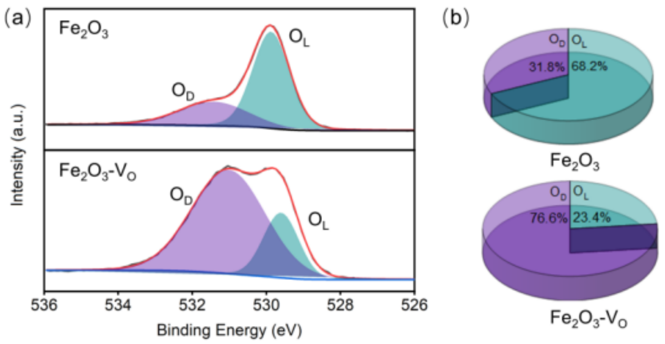

Figure 6. XPS characterization results of Fe_2O_3 nanofibers and Fe_2O_3 -VO

Subsequently, Fe_2O_3 nanofibers and Fe_2O_3 -V_O were applied to the oxidative degradation of two typical organic dyes, MB and RhB. At room temperature, Fe_2O_3 nanofibers and Fe_2O_3-V_O were added into a solution containing 50 ppm MB and RhB, respectively, and PMS was added as an oxidizing agent. The relative concentration of the two dyes (c/c0) under the action of catalysts as a function of time is shown in Figure 7. Catalyzed by Fe_2O_3 nanofibers, the concentration of MB decreased slowly with time, and the c/c0 was still about 80% when the reaction was carried out for 16 min, whereas the relative concentration of MB decreases significantly faster with the Fe_2O_3-V_O catalyst, reaching almost zero within the first four minutes, indicating a rapid and complete degradation. This extreme contrast brings out the better catalytic ability of Fe_2O_3-V_O, which is most probably explained by the availability of oxygen vacancies, which increase the catalytic activity and the more efficient degradation process of the methylene blue dye than the defect-free Fe_2O_3 catalyst.

The catalyst with defects of Fe_2O_3 is therefore shown to have a much higher efficiency in degradation during the experiment, with a steeper drop and a steadily lower relative concentration of methylene blue. In the case of RhB, also, the catalyst containing defects (blue line) is more effective in degrading RhB than the catalyst without defects (red line). The flawed catalyst will decrease concentration up to the point of close to zero at the end of the testing period, but the flawless catalyst will have less efficient degradation and will have a higher concentration of dye. The difference in the degradation efficiency observed implies that oxygen vacancy defects play a vital role in increasing the catalytic activity, which should be further investigated with regard to the effect they have on the overall catalyst performance. The beneficial aspect of defects is that the presence of defects in Fe_2O_3 catalysts increases their degradation abilities in such circumstances. Defects can either offer further active sites or affect the electronic structure in such a manner that is favourable to the catalytic reaction. This could be the generation of reactive oxygen species or increased adsorbing capacities. Besides the general performance, the kinetics of the degradation process give more information on the effectiveness and efficiency of the catalysts. It shows a fast initial activity, the steepness of the initial rise and fall of both catalysts implies that they are active at the beginning of the reaction, probably because of the presence of active sites and strong adsorption capacity. And it also maintained action with defects. It is not that the catalysts with defects do not display a significant plateau as fast as their defect-free counterparts, which implies that they retain their activity longer, and that could be because of a stronger mechanism, which takes advantage of the defects.

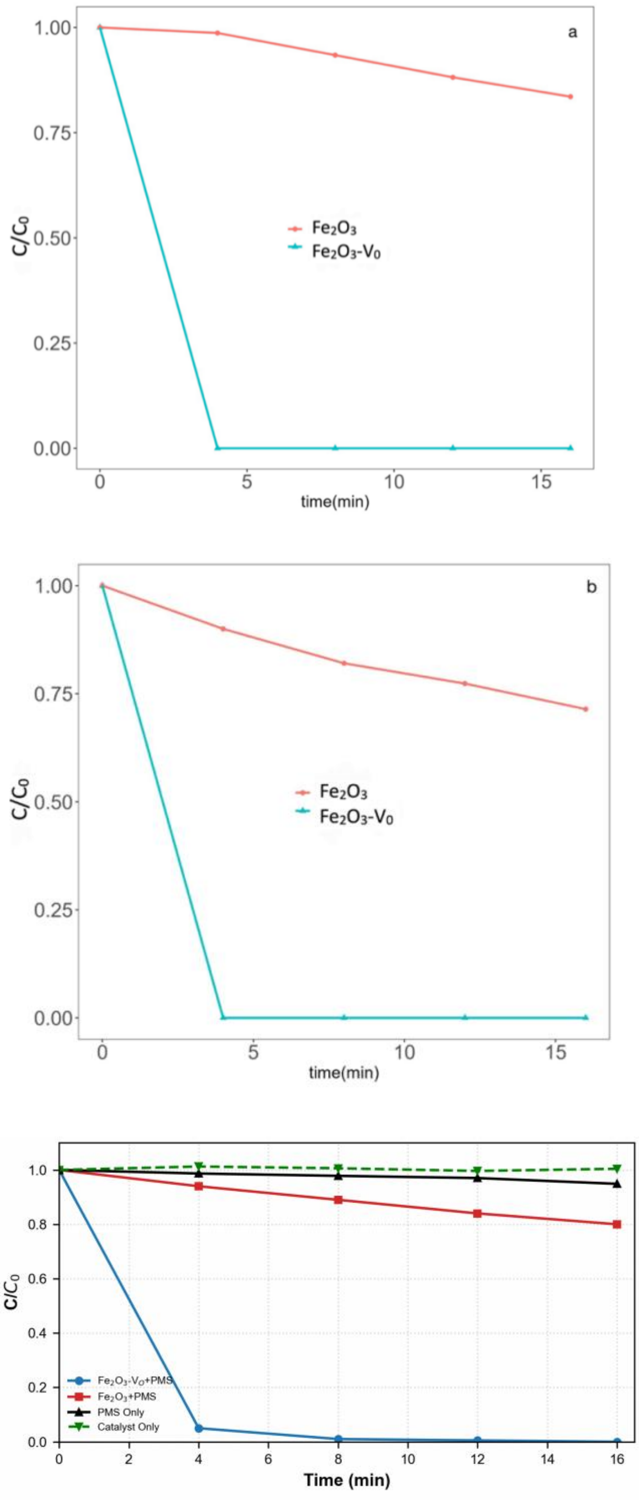

Figure 7. The c/c0 of reactants vs time of both Fe_2O_3 nanofibers and Fe_2O_3 -VO in the catalytic degradation of (a) MB and (b) RhB. (c) Control experiments comparing the degradation efficiency of Fe_2O_3 -V_(O)+PMS and Fe2O3 +PMS with PMS-only and Catalyst-only conditions.

Control experiments (Figure 7c) further confirmed this catalytic nature: neither “PMS Only” nor “Catalyst Only” conditions showed significant dye removal (<5%), proving that the rapid degradation is exclusively driven by the PMS activation on the defect-rich catalyst surface. Furthermore, the degradation kinetics were analyzed using a pseudo-first-order model ($\ln(C_0/C)=kt$). The calculated rate constant for Fe_2O_3-V_(O) (k≈0.95 min^{-1}) is approximately 68 times higher than that of pristine Fe_2O_3 (k≈0.014 min-1), quantitatively confirming the superior catalytic efficiency induced by oxygen vacancies.

The enhanced catalytic performance of Fe_2O_3-V_(O) can be fundamentally attributed to the modified electronic structure and surface chemistry induced by oxygen vacancies. Defects serve as electron-rich centers that facilitate the adsorption of PMS molecules and accelerate the electron transfer from the catalyst to the oxidant. This process promotes the cleavage of the O-O bond in PMS, leading to the efficient generation of reactive radicals. Based on the widely accepted radical pathway in iron-based advanced oxidation processes [2,17], the specific reactions are described in Eqs. (1)–(5):

$$\mathrm{Fe^{3+} + HSO_5^- \rightarrow Fe^{2+} + SO_5^{\cdot-} + H^+} \quad (1)$$

$$\mathrm{Fe^{2+} + HSO_5^- \rightarrow Fe^{3+} + SO_4^{\cdot-} + OH^-} \quad (2)$$

$$\mathrm{SO_4^{\cdot-} + H_2O \rightarrow SO_4^{2-} + \cdot OH + H^+} \quad (3)$$

$$\mathrm{SO_4^{\cdot-} + Organics \rightarrow Intermediates \rightarrow CO_2 + H_2O} \quad (4)$$

$$\mathrm{OH + Organics \rightarrow Intermediates \rightarrow CO_2 + H_2O} \quad (5)$$

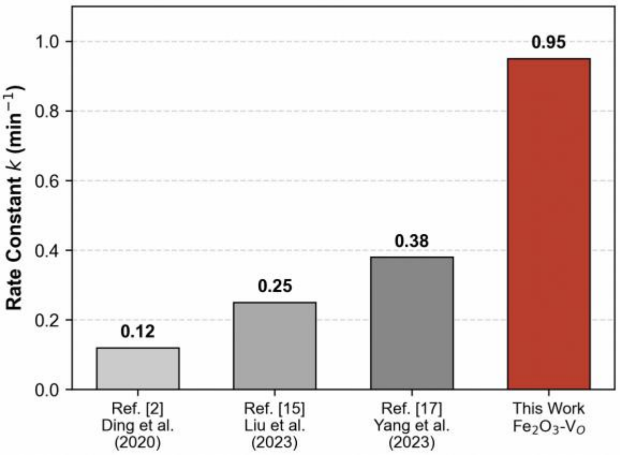

Figure 8. Comparison of the pseudo-first-order rate constants for organic dye degradation by Fe_2O_3-V_(O) in this work versus other Fe_2O_3-based catalysts reported in literature [2,15,17]

The reaction mechanism involves three key steps: (1) Adsorption: Engineered oxygen vacancies (V_O) facilitate the specific adsorption of PMS anions (HSO_5^-) onto the catalyst surface. (2) Activation: $V_O$accelerates the Fe^{3+}/Fe^{2+}redox cycle (Eqs. 1-2), typically the rate-determining step. Regenerated Fe^{2+}species then activate surface-bound PMS to generate reactive sulfate ($\cdot SO_4^-$) and hydroxyl ($\cdot OH$) radicals. (3) Degradation: These highly oxidizing radicals attack dye molecules, mineralizing them into $CO_2$and H_2O (Eqs. 4-5). High surface Fe^{2+}concentration induced by $V_O$is crucial for sustaining this radical generation cycle. To highlight performance, a comparison with other reported iron-based catalysts for PMS activation is presented in Figure 8. The Fe_2O_3-V_O nanofibers exhibit competitive degradation efficiency and kinetics, verifying the effectiveness of the oxygen vacancy engineering strategy.

4. Conclusion

Fe_2O_3 nanofiber was produced by the electrospinning method and high-temperature calcination. Oxygen vacancy defects were further constructed on the surface of Fe_2O_3 nanofibers by $NaBH_4$ reduction to obtain Fe_2O_3 -V_O. The formation of oxygen vacancy defects was confirmed by characterization methods, such as XRD, EPR, and XPS. Fe_2O_3 -V_O with oxygen vacancy defects showed much better catalytic performance when used as a catalyst in the oxidative degradation of organic dyes such as MB and RhB, indicating that the oxygen vacancy defect structure can help the activation of PMS for the efficient oxidative degradation of organic dyes. This finding provides a reference for the structural design of catalysts for the degradation of organic pollutants. This study underscores the importance of defect engineering in enhancing the catalytic efficiency of iron oxide nanofibers.

Ethical issue

The author is aware of and complies with best practices in publication ethics, specifically regarding authorship (avoidance of guest authorship), dual submission, manipulation of figures, competing interests, and compliance with research ethics policies. The author adheres to publication requirements that the submitted work is original and has not been published elsewhere.

Data availability statement

The manuscript contains all the data. However, more data will be available upon request from the authors.

Conflict of interest

The author declares no potential conflict of interest.

References

[1] Xiao, Z., Wu, R., Shu, T., Wang, Y., & Li, L. (2023). Synthesis of Co-doped Fe metal–organic framework MIL-101 (Fe, Co) and efficient degradation of organic dyes in water. Separation and Purification Technology, 304, 122300. https://doi.org/10.1016/j.seppur.2022.122300

[2] Ding, J., Pan, Y., Li, L., Liu, H., Zhang, Q., Gao, G., & Pan, B. (2020). Synergetic adsorption and electrochemical classified recycling of Cr(VI) and dyes in synthetic dyeing wastewater. Chemical Engineering Journal, 384, 123232. https://doi.org/10.1016/j.cej.2019.12323.

[3] Yu, X., Zhang, J., Chen, Y., Ji, Q., Wei, Y., Niu, J., Yu, Z., & Yao, B. (2021). Ag-Cu2O composite films with enhanced photocatalytic activities for methylene blue degradation: Analysis of the mechanism and the degradation pathways. Journal of Environmental Chemical Engineering, 9(4), 106161. https://doi.org/10.1016/j.jece.2021.106161

[4] Fan, L., Su, X., Zhu, H., Liu, H., Lou, S., Shi, Y., & Yan, S. (2023). Degradation of Methylene Blue by Hot Electrons Transfer in SnSe. Advanced Materials Interfaces, 10(11), 2202207. https://doi.org/10.1002/admi.202202207

[5] Kong, L.-H., Wu, Y., Shen, R.-F., Zhang, W.-J., Dong, Z.-Y., Ge, W.-T., Guo, X.-J., Yan, X., Chen, Y., & Lang, W.-Z. (2022). Combination of N-doped porous carbon and g-C_3N_4 for effective removal of organic pollutants via activated peroxymonosulfate. Journal of Environmental Chemical Engineering, 10(3), Article 107808. https://doi.org/10.1016/j.jece.2022.107808

[6] Chen, Q., Ning, S., Yang, J., Wang, L., Yin, X., Wang, X., ... & Zeng, D. (2024). In situ interfacial engineering of CeO2/Bi2WO6 heterojunction with improved photodegradation of tetracycline and organic dyes: mechanism insight and toxicity assessment. Small, 20(18), 2307304. https://doi.org/10.1002/smll.202307304

[7] Rahimi, A. A., & Alihosseini, F. (2024). In Vivo and In Vitro Decolorization of Disperse Azo Dyes Using Aspergillus niger. Journal of Environmental Engineering, 150(9), 04024041. https://doi.org/10.1061/joeedu.eeeng-7596

[8] Moumen, A., Belhocine, Y., Sbei, N., Rahali, S., Ali, F. A. M., Mechati, F., Hamdaoui, F., & Seydou, M. (2022). Removal of malachite green dye from aqueous solution by catalytic wet oxidation technique using Ni/Kaolin as catalyst. Molecules, 27(21), 7528. https://doi.org/10.3390/molecules27217528

[9] Fang, D., Luo, D., Xiao, H., Li, J., Ma, L., Zi, J., & Lian, Z. (2024). Oxygen Vacancies-Mediated Z-Scheme Mechanism Promotes Synergistic Photoelectrocatalysis for Hydroxyl Radical and Singlet Oxygen-Cooperating on Selective Pollutant Degradation. ACS ES&T Engineering, 5(1), 77-85. https://doi.org/10.1021/acsestengg.4c00453.s001

[10] Yanardağ, D., & Edebali, S. (2024). Adsorptive removal of dyes from aqueous solutions using biomass-derived activated carbon. Biomass Conversion and Biorefinery, 14, 5699–5712. https://doi.org/10.1007/s13399-023-04839-w

[11] Ye, H., Chen, D., Li, N., Xu, Q., Li, H., He, J., & Lu, J. (2021). Polymer of intrinsic microporosity coated on a metal-organic framework composite membrane for highly efficient dye separation. Journal of Membrane Science, 637, 119619. https://doi.org/10.1016/j.memsci.2021.119619

[12] Zheng, H., Lu, H., Li, S., Niu, J., Leong, Y. K., Zhang, W., ... & Chang, J. S. (2024). Recent advances in electrospinning-nanofiber materials used in advanced oxidation processes for pollutant degradation. Environmental Pollution, 344, 123223. https://doi.org/10.1016/j.envpol.2023.123223

[13] He, Z., Ong, J. H., Bao, Y., & Hu, X. (2023). Chemocatalytic membranes for efficient degradation of emerging organic contaminants. Journal of Environmental Chemical Engineering, 11(3), 109548. https://doi.org/10.1016/j.jece.2023.109548

[14] Liu, Y., Han, W. K., Chi, W., Fu, J. X., Mao, Y., Yan, X., & Gu, Z. G. (2023). One-dimensional covalent organic frameworks with atmospheric water harvesting for photocatalytic hydrogen evolution from water vapor. Applied Catalysis B: Environmental, 338, 123074. https://doi.org/10.1016/j.apcatb.2023.123074

[15] Liu, H., Li, X., Zhang, X., Coulon, F., & Wang, C. (2023). Harnessing the power of natural minerals: a comprehensive review of their application as heterogeneous catalysts in advanced oxidation processes for organic pollutant degradation. Chemosphere, 337, 139404. https://doi.org/10.1016/j.chemosphere.2023.139404

[16] Jiménez-González, C., Gil-Calvo, M., de Rivas, B., González-Velasco, J. R., Gutiérrez-Ortiz, J. I., & López-Fonseca, R. (2016). Oxidative steam reforming and steam reforming of methane, isooctane, and N-Tetradecane over an alumina supported spinel-derived nickel catalyst. Industrial & Engineering Chemistry Research, 55(14), 3920-3929. https://doi.org/10.1021/acs.iecr.6b00461.s001

[17] Yang, H., Li, G., Jiang, G., Zhang, Z., & Hao, Z. (2023). Heterogeneous selective oxidation of VOCs over transition metal catalysts. Applied Catalysis B: Environmental, 325, 122384. https://doi.org/10.1016/j.apcatb.2023.122384

[18] Khan, W. U., Hantoko, D., Bakare, I. A., Al Shoaibi, A., Chandrasekar, S., & Hossain, M. M. (2024). Co-Ni catalysts supported on zirconia for syngas production. Fuel, 369, 131675. https://doi.org/10.1016/j.fuel.2024.131675

[19] Xie, Z., Sun, Z., Shao, B., Zhu, Y., Ma, R., Li, S., ... & Hu, J. (2024). Highly efficient hydrogenation of carbonate to methanol for boosting CO2 mitigation. Chemical Engineering Journal, 495, 153465. https://doi.org/10.1016/j.cej.2024.153465

[20] Xie, C., Niu, Z., Kim, D., Li, M., & Yang, P. (2020). Surface and Interface Control in Nanoparticle Catalysis. Chemical Reviews, 120(2), 1184–1249. https://doi.org/10.1021/acs.chemrev.9b00220

[21] Li, Z., Ji, S., Liu, Y., Cao, X., Tian, S., Chen, Y., Niu, Z., & Li, Y. (2020). Well-Defined Materials for Heterogeneous Catalysis: From Single Atoms to Clusters and Nanoparticles. Chemical Reviews, 120(2), 623–682. https://doi.org/10.1021/acs.chemrev.9b00311

[22] Geng, Y., Lian, Z., Zhang, Y., Liu, J., Jin, D., & Shan, W. (2024). Heteropoly acid-grafted catalysts for efficient NOx reduction. Catalysis Science & Technology, 14, 3064–3072. https://doi.org/10.1039/D4CY00210E

[23] Xiang, Z., Wang, W., Zhou, F., Zhang, H., Wang, Y., Zhu, W., & Wang, H. (2024). Efficient conversion of lignin-derived phenols to cycloalkanes over bifunctional catalysts with low loading of ruthenium. Fuel Processing Technology, 256, 108073. https://doi.org/10.1016/j.fuproc.2024.108073

[24] Shu, D., Long, X., Zhao, P., Wang, L., Li, Z., Cheng, C., ... & Cheng, B. (2024). Flash spinning polyethylene/Fe3O4 magnetic drive fibers for oil absorption underwater. Chemical Engineering Journal, 490, 151333. https://doi.org/10.1016/j.cej.2024.151333

[25] Xu, Z., Liu, Y., Sun, X., Xie, X., Guan, X., Chen, C., & Ma, X. (2022). Theoretical design of Na-rich anti-perovskite as solid electrolyte: The effect of cluster anion in stability and ionic conductivity. Journal of Solid State Chemistry, 316, 123643.https://doi.org/10.1016/j.jssc.2022.123643

[26] Li, Y., Han, B., Bi, F., Wu, Z., & Weng, X. (2024). One-Pot Synthesis of (CrMnFeCoNi) O x High-Entropy Oxides for Efficient Catalytic Oxidation of Propane: A Promising Substitute for Noble Metal Catalysts. ACS Applied Materials & Interfaces, 16(48), 66108-66116. https://doi.org/10.1021/acsami.4c14292.s001

[27] Wu, Y., Ma, L., Wu, J., Song, M., Wang, C., & Lu, J. (2024). Mesoporous Sc2O3 for Biomass Valorization to Fine Chemicals. Advanced Materials, 36(15), e2311698. https://doi.org/10.1002/adma.202311698

[28] Chen, L., Zou, Y., Li, Y., Li, G., Liu, W., Zhang, H., & Peng, H. (2024). Alkali-resistant catalytic reduction of NOx over CeO2-WO3/MCM-22 supported catalyst by releasing Brønsted acid sites. Applied Catalysis B: Environment and Energy, 347, 123788.https://doi.org/10.1016/j.apcatb.2024.123788

[29] Sun, J., Xia, W., Zheng, Q., Zeng, X., Liu, W., Liu, G., & Wang, P. (2020). Increased active sites on α-Fe2O3 for enhanced photo-Fenton catalytic activity. ACS Omega, 5(21), 12339–12347. https://doi.org/10.1021/acsomega.0c01072

[30] Zhang, N., Li, X., Liu, Y., Long, R., Li, M., Chen, S., Qi, Z., Wang, C., Song, L., Jiang, J., & Xiong, Y. (2017). Defective Tungsten Oxide Nanosheets for Efficient Photocatalytic Hydrogen Evolution. SmallSmall, 13(33), 1701354. https://doi.org/10.1002/smll.201701354

[31] Liu, H., Yang, F., Xiang, M., Cao, Y., & Wu, T. (2021). Development of multilayer polypropylene separators for lithium-ion batteries via an industrial process. Industrial & Engineering Chemistry Research, 60(30), 11611-11620. https://doi.org/10.1021/acs.iecr.1c01577

[32] Cen, S., Li, L., Li, Y., Wan, C., Linghu, W., & Wang, L. (2024). Low-Temperature Catalytic Transfer Hydrogenation of Biomass-Derived Furfural over Irreversibly Adsorbed and Highly Dispersed Zr (IV) Species. Inorganic Chemistry, 63(29), 13775-13784. https://doi.org/10.1021/acs.inorgchem.4c02156.s001

[33] Zhuang, L., Ge, L., Yang, Y., Li, M., Jia, Y., Yao, X., & Zhu, Z. (2017). Ultrathin Iron-Cobalt Oxide Nanosheets with Abundant Oxygen Vacancies for the Oxygen Evolution Reaction. Advanced Materials, 29(17), 1606793. https://doi.org/10.1002/adma.201606793